Acta Materialia 254 (2023) 119015

Contents lists available at ScienceDirect

Acta Materialia

journal homepage: www.elsevier.com/locate/actamat

Full length article

Sintering inhibition enables hierarchical porosity with extreme resistance to degradation during redox cycling of Fe-Mo foams

Jacob B. Mack [*,1], Samuel M. Pennell, David C. Dunand

Department of Materials Science and Engineering, Northwestern University, Evanston, IL 60208, USA

ARTICLE INFO

Keywords:
Hydrogen
Sintering
Freeze-casting
Porosity
Redox cycling

ABSTRACT

High-temperature (800 °C) steam-hydrogen redox cycling, relevant to grid-scale energy storage, is studied for iron-based freeze-cast lamellar foams. In contrast to previously studied Fe, Fe-Ni, and Fe-Co foams that rapidly degrade, Fe-25Mo foams feature a much-enhanced structural damage resistance. Utilizing *in-situ* x-ray diffraction, microscopy, and x-ray tomography, strong sintering inhibition is observed in Fe-Mo foams, creating a hierarchically porous lamellar structure. This leads to (i) wide channels between lamellae, enabling high macroscopic porosity (~78%) which can accommodate gas flow as well as volumetric expansion without lamellar contact, and (ii) microporosity within lamellae, providing additional free volume to accommodate expansion during oxidation, limiting both swelling of the lamellae and the formation of Kirkendall pores. These combined effects enable a near-complete reversibility of the microstructure during cycling, preventing damage produced *via* internal lamellar buckling, cracking, contacting and sintering, with a remarkably high porosity (65%) remaining after 50 consecutive redox cycles.

1. Introduction

Redox-active Fe-based materials, operating in tandem with a reversible solid-oxide fuel cell, hold significant promise towards environmentally-friendly, inexpensive, grid-scale energy storage, capable of mitigating the intermittency of solar and wind power generation [1–5]. For rapid charging and discharging of this iron-air battery (with overall reaction: $3Fe + 2\ O_2 \leftrightarrow Fe_3O_4$), the reversible solid-oxide fuel cell and the Fe material must be operated at elevated temperatures (500 – 800°C) to achieve favorable redox kinetics [6–8]. In discharging mode, iron is oxidized by steam to liberate hydrogen ($3Fe + 4\ H_2O \rightarrow Fe_3O_4 + 4\ H_2$), which combines in the fuel cell with oxygen from the air to produce current; the produced steam is cycled back to the iron. To recharge, the reverse reaction takes place, as iron oxide is reduced by hydrogen created by the fuel cell in electrolysis mode with steam again cycling internally. However, a 110% molar volume expansion is associated with the $Fe \rightarrow Fe_3O_4$ oxidation reaction.

In Fe powder beds, commonly used for their high surface area, this volumetric expansion combined with high operating temperatures leads to extensive and rapid powder sintering, which creates large, dense regions that greatly slow reaction speed by increasing the diffusion distance for unreacted material and by limiting gas access to interior surfaces, limiting the reversibility and lifetime of the material [9–12]. To address this issue, researchers have studied two main strategies: (i) assembling the Fe particles into geometries different from packed powder beds, and (ii) alloying Fe particles to mitigate sintering and/or enhance redox kinetics.

For the first strategy, water-based freeze casting – an environmentally-friendly and scalable manufacturing method - has shown promise for creating functional, porous structures [13,14]. Our previous work has demonstrated that freeze casting can produce highly-porous lamellar Fe-based foams with internal porosity capable of accommodating the redox volumetric changes, so as to decrease sintering tendencies [15]. However, rapid degradation still persists in these foams, stemming from the formation of Kirkendall porosity during oxidation, due to the mismatch in Fe out-diffusivity and O in-diffusivity [16]. This leads to microporosity forming at the cores of lamellae, which, combined with stresses due to volumetric expansion and brittleness of the oxide, triggers lamellar fracture and swelling. Microporosity formation seen in our foams is additionally consistent with prior literature on iron oxidation [17–19]. As a result, in our lamellar foams, contact occurs between neighboring lamellae, which triggers sintering

* Corresponding author.
E-mail address: jacobmack2022@u.northwestern.edu (J.B. Mack).
[1] Present address: Massachusetts Institute of Technology, Cambridge MA 02139, USA.

https://doi.org/10.1016/j.actamat.2023.119015
Received 17 January 2023; Received in revised form 5 April 2023; Accepted 13 May 2023
Available online 15 May 2023

at the point of contact. This densification mechanism eventually chokes the inter-lamellar channels of the foam, eliminating the porous structure and hindering reaction speed by the same mechanisms observed in packed powder beds [11]. This process is exacerbated on the exterior envelope of the foam, where lamellae edges are subjected to stress concentrations during redox cycling, leading to the formation of a dense shell that encapsulates the foam, which limits, and ultimately eliminates, gas flow into and out of the foam interior volume [20].

The second strategy, based on alloying Fe-based systems, focuses on two separate approaches: (i) increasing sintering resistance of Fe-particles, and (ii) increasing the redox reaction rates, which enables a lower operating temperature and thus a lower rate of sintering. Common sintering inhibitors include stable, redox-inactive oxides (Al_2O_3, CeO_2, SiO_2, ZrO_2), which have significant promise in increasing the lifetime of the redox-active Fe material, but lead to lower specific redox capacity and higher cost [11,21–23]. Among metallic additives, Sc, Ti, V, Cr, and Mo stabilize Fe-particles in powder beds over numerous redox cycles, with Mo showing the strongest sintering mitigation during prolonged cycling [22,24]. Other metallic additives (i.e., Mn, Co, Ni, Cu, Ga, Nb, W, and Re) act as kinetic limiters during oxidation due to promotion of sintering, commonly forming solid solutions which accelerates the sintering [22]. The addition of Mo, as well as noble metals (Ru, Rh, Pd, Ag, Ir, Pt), catalyze the redox reaction of Fe and lower the minimum feasible operating temperature. The relatively low cost of Mo (especially in ferromolybdenum form) [25], and its ability to act both as a sintering inhibitor and kinetic catalyst, make it attractive as alloying addition to Fe. The catalytic effect of Mo on Fe oxidation is well studied, stemming from the changing cation valance of Mo, resulting in significant redox reactivity at temperatures as low as 300°C [26,27]. So far, these alloying studies focus on the dilute additions of alloying elements, commonly 0 – 5 vol %, in powder bed systems.

Combining alloying and structuring, our previous work has explored the effects of oxide (CeO_2 and ZrO_2) [28] and metallic (Cu, Co, and Ni) [29–31] additives in freeze-cast Fe-based foams. While the addition of 5-15 vol% sintering oxide inhibitors prevents most of the volumetric shrinkage for foams over their first five redox cycles, this effect is temporary. During extended cycling, the redox-inactive inhibitor particles segregates to the core of the lamellae. Thereafter, Fe segregated at the lamellar surface follows the same degradation mechanisms observed for pure Fe foams. Alloying of Fe with Cu leads to a similar outcome: while the Cu-phase catalyzes the oxidation, it becomes segregated to the lamellar interior after a few redox cycles, as it is immiscible with Fe, leading to rapid densification of the lamellae as their surface becomes devoid of any Cu.

Additives which are soluble in Fe (e.g., Ni and Co) behave very differently in lamellar, freeze-cast Fe-Ni or Fe-Co foams. These redox inactive alloying elements form a continuous metallic Ni- or Co-rich core in each lamella during oxidation, providing an additional interface for vacancy removal, thus decreasing Kirkendall pores. Also, the metallic, ductile core provides mechanical adhesion to the oxide layer, limiting fracture and spallation of the lamellae during oxidation. After reduction of the lamellar outer shells to Fe, interdiffusion with Ni and Co in the cores leads to lamellae re-homogenization to a uniform Fe-Ni or Fe-Co solid solution, allowing the redox process to be microstructurally reversible. This allows for significant (> 40%) interlamellar channel porosity to be maintained in the freeze-cast foam over 10 redox cycles. The improved porosity retention of Fe-Ni and Fe-Co foams, driven by their microstructural evolution, indicates that the requirements for increasing foam lifetime differ significantly from those of powder-bed systems. Beyond 10 cycles, however, irreversible internal plastic deformation builds up in the form of lamellar buckling, leading to increased contact points between neighboring lamellae and sintering.

With this knowledge base, we study here alloying of lamellar iron foams with molybdenum, to further decrease (as compared to Fe-Ni and Fe-Co foams) degradation under steam-hydrogen redox cycling which is driven by lamellar sintering and buckling, and the formation of Kirkendall porosity. Fe-Mo alloys, beside their known catalytic activity for redox cycling in packed powder beds [26,27], exhibit two terminal solid solutions with extensive solubility (α-Fe(Mo) and α-Mo(Fe)), together with various intermetallic compounds, unlike the Fe-Ni and Fe-Co systems which show a continuous solid solution at elevated temperatures. Utilizing previous *ex-* and *in-situ* methods to analyze Fe-25Ni, Fe-25Co and Fe-25Cu (at%) lamellar foams [30,31], we investigate here the chemical and phase evolution of Fe-25Mo (at%) lamellar foams during redox cycling, focusing on the microstructural evolution and the mechanisms of sintering inhibition during long-term steam-hydrogen redox cycling. We demonstrate a remarkable compositional and structural reversibility of lamellar Fe-25Mo foams up to 50 redox cycles, despite the large volumetric expansion during oxidation and the phase separation occurring as Fe and Mo oxidize. We show that the exceptional ability of Mo to inhibit Fe sintering is responsible for this very high redox stability in lamellar Fe-25Mo foams.

2. Experimental

2.1. Foam Synthesis

Lamellar Fe-Mo foams were fabricated *via* a water-based freeze casting technique, detailed in our previous work, with minor modifications [15]. In summary, an aqueous slurry is created, combining precursor oxide powders of α-Fe_2O_3 (Noah Technologies, 99.9%, < 3 μm average), MoO_3 (US Research Nanomaterials, 99.9%, 6 μm), with Zephrym PD 4974 dispersant (Croda, Inc.). The volume fraction of oxide powders and Zephrym in the slurry are 10 and 0.5%, respectively. The mass ratio of Fe_2O_3 to MoO_3 is 1.66, yielding an atomic ratio of 3 (i.e., Fe–25Mo) after reduction. The slurry was ball milled for 48 h with zirconia milling media (12 mm balls, equal volumes of media and slurry) to eliminate agglomerates in the oxide particles. Polyethylene glycol (M_n=3350, Sigma Aldrich), used as a binder, was then dissolved in additional DI water, representing 2 vol% of the slurry. Modifications for altering freeze-cast wavelength are detailed in Section S1.

The oxide powder suspension was then degassed under mechanical vacuum, and chilled to 0 °C (without freezing) in an ice bath prior to freeze casting. A copper plate was then chilled to 1 °C *via* a thermoelectric device attached to its underside; a cylindrical Teflon mold (height of 15 mm, inner diameter of 15 mm, outer diameter of 25 mm), pre-chilled to 0 °C, was placed on top of the copper plate, using vacuum grease to ensure the mold maintains a good contact with the plate. The entire apparatus was surrounded by Styrofoam insulation to limit radial temperature gradients. A 2 mL volume of chilled slurry was then pipetted into the mold, and the copper plate was cooled to -30 °C following an exponential cooling curve yielding a constant freeze-casting velocity of 16 μm/s [32]. The frozen sample was then punched out of the Teflon mold, and the bottom 1–2 mm frozen sedimentation layer was removed by cutting with a chilled razor blade. The resulting cylindrical specimen (12 mm in height and 15 mm in diameter) was placed on an alumina plate and freeze-dried under vacuum (0.13 mbar) at -54 °C for 48 h to sublimate the ice. After sublimation, the green body foam was transferred to a furnace, where the binder was burned out at 300 °C for 1 h, the oxide powders were reduced at 600 °C for 4 h, and the lamellae were sintered at 1000 °C for 3.5 h, all under flowing H_2 (Airgas, UHP). Heating and cooling rates were 10 and 5 °C/min, respectively. The resulting metallic Fe-25Mo foams appeared light grey and shrunk significantly, showing a final diameter of 12–13 mm and height of 8–9 mm.

2.2. Foam Redox Cycling and Characterization

Redox performance of foams was studied *via* consecutive steam and hydrogen exposure (redox cycle) to simulate operating conditions. Foams are placed on an alumina plate and ramped to 800 °C at 10 °C/min under flowing H_2 (100 sccm) to maintain the metallic state of the

foam. After the furnace equilibrates at 800 °C, the first oxidation half cycle begins, where Ar is flowed (120 sccm) through a 93 °C water bubbler, achieving a H_2O steam partial pressure of 0.77 atm. All gas lines were heated to 110 °C to prevent any steam condensation. After the first 120 min oxidation half-cycle, H_2 is flowed (200 sccm) for 90 min for the reduction half cycle. Cycles are repeated with either 60 or 90 mins of oxidation, followed by 90 mins of reduction: these cycle times are chosen to ensure full oxidation and full reduction. Following the last reduction cycle, foams are cooled at 5 °C/min under flowing H_2 (100 sccm) to maintain the metallic state after cooling. When a foam is partially cycled (i.e., when cycling is interrupted before the end of the reduction half-cycle), it is instead cooled under flowing Ar-4% H_2 to prevent further oxidation while maintaining any oxide present. Foams are weighted after cycling to calculate oxygen gains if the sample is in an oxidized state, or to ensure that the foam is fully reduced.

After cycling, foams are vacuum-mounted in epoxy (Epothin 2, Buehler), and polished to halfway through their height. The final polishing step of the full radial cross-section is done with a 1 μm diamond suspension. For partially oxidized foams, an additional ion milling step on a LEICA TIC3X is performed to remove polishing damage to the oxidized layer and reveal internal porosity. The radial cross sections are imaged on an optical microscope (MA200, Nikon), by stitching together multiple 5x magnification images. The microscope is refocused every 4 pictures. To analyze the cross-section, the images are processed using the ImageJ software. First, the cross-section is converted to a binary image, with lamellae treated as 1 and channels 0. A median filter (radius of 1 pixel) is applied to reduced and sintered foams to eliminate intra-lamellar porosity. Foam porosity is calculated from solid fraction, taken as the ratio of lamellae area to total sample area. Lamellar thickness is calculated by deploying the local thickness algorithm in ImageJ [33]. Interlamellar channel width is calculated *via* the local thickness plugin on the inverse of the filtered image described above, shown in Fig. S1. The structural parameters calculated through this analysis of cross-sections were previously shown to be in good agreement with those determined by 3-d X-ray computed tomography [16].

Scanning electron microscopy (SEM) and energy-dispersive x-ray spectroscopy (EDS) imaging were performed on Hitachi 8030 and JEOL JSM-7900FLV SEM instruments, using a 15kV accelerating voltage. Epoxy-mounted foams were sputter-coated with a 10 nm Au-Pd film, while unmounted foams were imaged without coating. Carbon content was analyzed *via* combustion analysis, in accordance with ASTM E1019-18 (C) by Westmoreland Mechanical Testing & Research (Youngstown, PA).

2.3. Operando and Ex-situ X-ray Diffraction

Operando X-ray diffraction spectra recorded during redox cycling were collected in a similar setup to our previous work, with minor modifications [31,30]. Spectra were collected on a Stadi-MP (Stoe, Germany) instrument, with an asymmetric curved germanium monochromator under pure Ag-K_{a1} radiation (λ = 0.5594 Å) and a one-dimensional silicon strip-detector (MYTHEN2 1k, from Dectris, Switzerland), operated at 40 kV and 40 mA (Beam Size 4×0.8 mm). Data were collected in Debye-Scherrer (transmission) geometry, using 1-minute scans with 2θ between 5.7 and 24.3°, after calibration against a NIST Si standard (640d). A colony of lamellae was extracted, using a razor blade, from a reduced and sintered Fe-25Mo foam, measuring 1–1.5 mm in height and 1 – 1.5 mm in thickness. The lamellae were introduced in a 1.5 mm diameter quartz capillary and surrounded on both sides by amorphous quartz wool. On the inlet side, a small volume of Ni felt was added as an O_2 getter. The remainder of the capillary volume on the outlet side of the sample was filled with porous ceramic blocks to prevent sample movement upon changes in gas flow. The capillary was installed into a water-cooled, graphite-heated furnace, with temperature stability of 0.1 °C.

The experiment began by heating the sample to 800 °C at 30 °C/min, under flowing Ar-4% H_2, to ensure the sample remained metallic until the cycling temperature was reached. Once at 800 °C, the gas was switched to Ar, bubbled through a 40 °C bubbler (P_{sat} = 0.073 atm) for oxidation. All gas lines between the bubbler and capillary were heated to at least 40 °C to prevent steam condensation. Following complete oxidation, noted by unchanging diffraction patterns, Ar-4% H_2 was flowed for reduction. This procedure was repeated for two consecutive oxidation-reduction cycles. Processing of diffraction patterns was done in Python, with waterfall plots of diffraction spectra, after background correction with a modified polynomial fit [34], rendered *via* the Cmocean package [35]. Diffraction peaks, indexed using reference patterns from the Inorganic Crystal Structure Database (ICSD), were fitted to a Pseudo-Gaussian model using the limfit package [36]. These fitted peak were then integrated to achieve an area, expected to be proportional to the volume of the diffracting phase, and then normalized to the respective maxima of each phase.

Ex-situ X-ray diffraction spectra were gathered in transmission, by grinding portions of foams into powder with mortar and pestle. Measurements were done at room temperature on a STOE-STADI-P powder diffractometer, equipped with an asymmetric curved germanium monochromator (Cu Kα1 radiation, λ = 1.54056Å) and one-dimensional silicon strip detector (MYTHE2 1K from DECTRIS). The line-focused Cu X-ray tube was operated at 40 kV and 40 mA. Powder was packed in an 8 mm wide metallic mask and sandwiched between two acetate layers of tape. Intensity data for 2θ values between 15 and 75° were collected over a period of 90 min. The instrument was calibrated with a NIST Si standard (640d) prior to the measurement. Processing of diffraction patterns was done in Python, and background correction was performed using a modified polynomial fit [34]. Powder patterns were indexed using reference patterns from the ICSD and phase fractions were determined from Rietveld Refinement using GSAS-II [37].

2.4. Tomography

Synchrotron X-ray tomography was performed at Sector 5BM-C of the Advanced Photon Source (Argonne National Lab, IL). Epoxy-mounted foams were cut into 1 mm^3 cubes and placed on a rotational stage. Transmitted radiograms, using a monochromatic 36 keV X-ray beam, were imaged *via* a YAG phosphor detector (with 5 μm active layer) and recorded with a cryo-cooled CCD camera (Princeton Instruments/ Roper Scientific, 24 μm 16-bit pixels) over a rotation range of 0 – 180 °. A 10x objective was used, giving a (2.4μm) ^{3} voxel. 3D reconstructions were processed *via* ImageJ. After cross sections were converted to 8-bit and thresholded, outliers were removed, and the 3D viewer plugin was used to render the reconstruction.

3. Results & discussion

3.1. As-sintered foams

For this study, an Fe-25Mo (at%) composition was chosen because the 3:1 stoichiometry showed the best long-term performance in other alloy systems studied [29]. During fabrication, Fe-25Mo foams were subject to sintering for 240 min at 1000 °C. The resulting foams feature flat, unbuckled lamellae (Fig. 1a): the higher mechanical strength provided by Mo, as compared to unalloyed Fe, allows the Fe-Mo lamellae to resist plastic deformation during reduction- and sintering-induced foam shrinkage, as also observed in Fe-Ni foams [38]. Alloying with Mo also leads to significant macroscopic sintering inhibition of the foams during the initial reduction and sintering steps: Fe-Mo foam diameter shrinks from 15 mm (in the freeze-cast green state) to 11.5–12 mm (after sintering), as compared to 8.5 – 9 mm for Fe, Fe-Ni, and Fe-Co foams [15, 30,31]. This results in a higher initial porosity of 75-80%, compared to 62–70%. The sintering inhibition is also seen in the Fe-Mo foam microstructure, where lamellae are only partially sintered, as illustrated in Fig. 1b, creating a hierarchical porous structure: centimeter-long

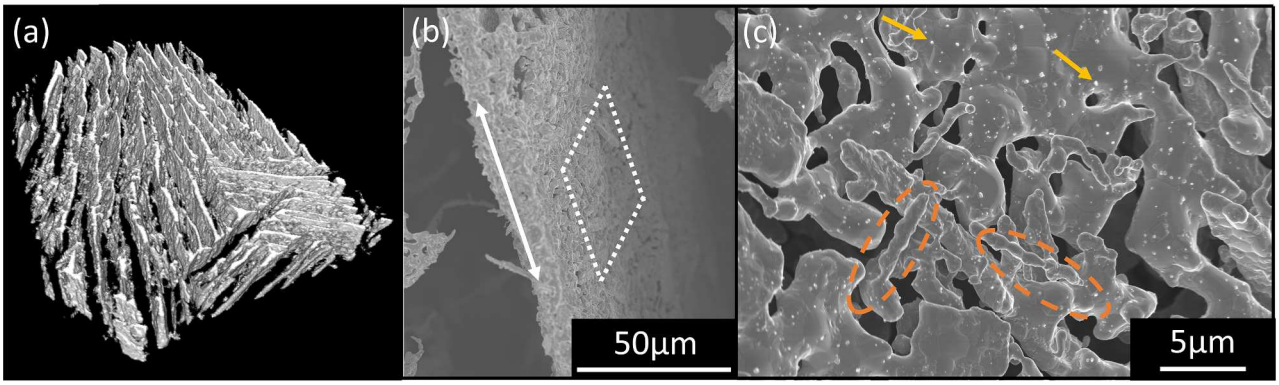

Fig. 1. Fe-25Mo foam after freeze-casting, reduction and sintering: (a) subsection of tomographic reconstruction (height of reconstructed region is 180 μm) showing lamellae and channels at low magnification; (b) SEM micrograph of porous lamella (white arrow shows freezing direction) at intermediate magnification; (c) porous surface of lamella (example section shown as dashed square in (b)), with orange circles highlighting needle-like regions and yellow arrows showing submicron particles (white contrast) identified as stable oxide impurities.

interlamellar channels from freeze casting and intra-lamellar microporosity from sintering inhibition. Parallel to the freezing direction, needle-like structures are also seen within the lamellae, as highlighted in Fig. 1c (orange outline). Finally, submicron bright particles - observed *via* EDS to be rich in Si, Mg, and Al - are expected to be impurity oxides, present in the initial Fe- and Mo-oxide precursor particles, as reported previously [39]; their low volume fraction and inertness makes them inconsequential for the redox behavior of the Fe-Mo foams.

The lamellar microporosity is visible in a representative lamellar cross section, as shown in Fig. 2a. A corresponding XRD pattern (Fig. 2b) shows the presence of three distinct phases: (i) α-Fe(Mo) solid solution with a BCC crystal structure (expected to contain ~3 at% Mo, the solid-solubility limit of Mo in Fe at 800 °C), (ii) Fe-rich μ-phase, with composition close to μ-Fe_3Mo_2 (isostructural with μ-Fe_7W_6), and (iii) a mixed Fe-Mo carbide, Fe_3Mo_3C, with a FCC crystal structure (Fig. 2b). The most prevalent phase is the α-Fe(Mo) phase, representing 51.5 mol

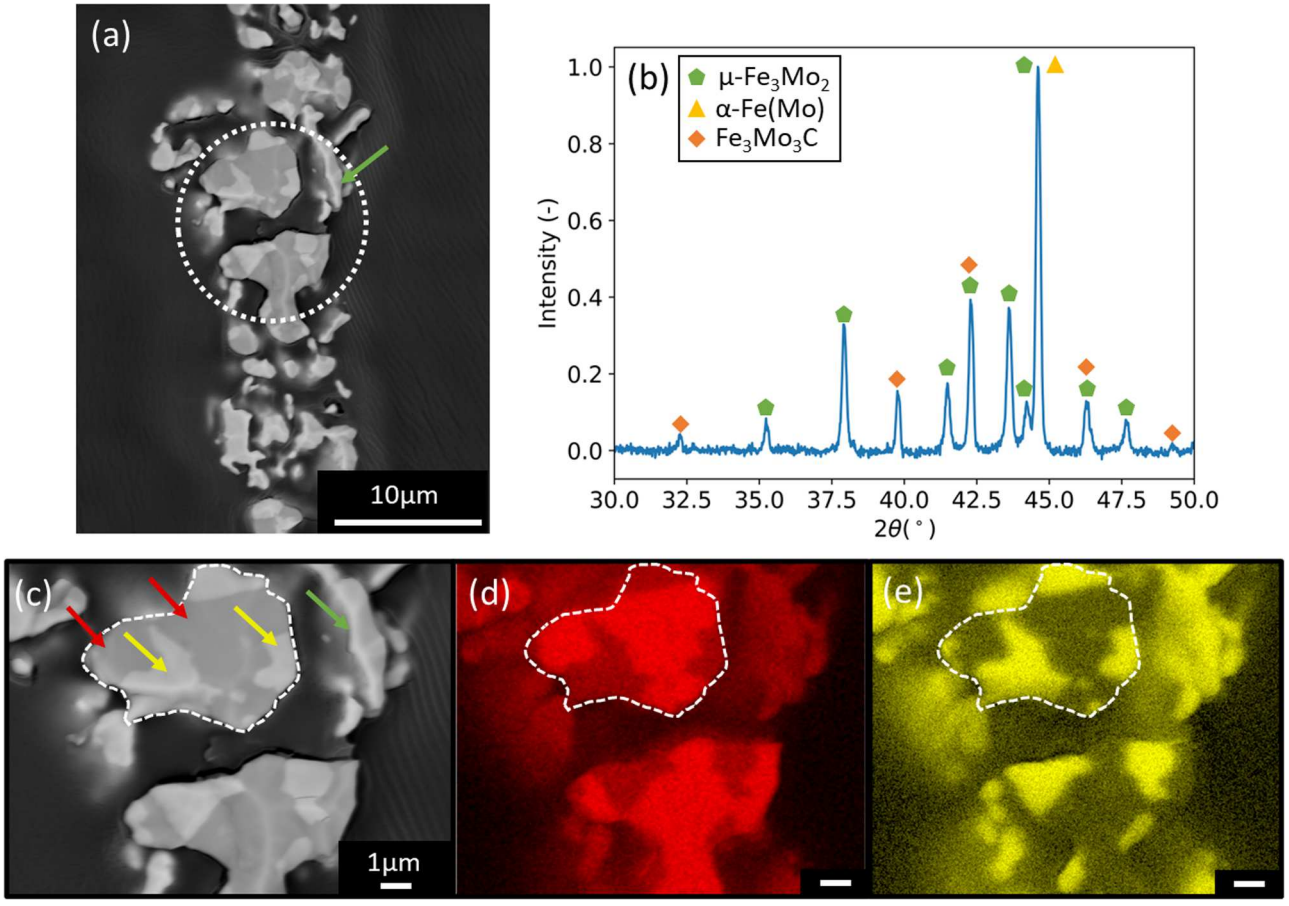

Fig. 2. As-processed Fe-25Mo foam (after freeze-casting, reduction and sintering) (a) Cross sectional view of porous metallic lamella, imaged via back-scattered SEM; (b) XRD pattern showing coexistence of α-Fe(Mo), μ-Fe_3Mo_2, and FCC- Fe_3Mo_3C phases; (c) high-magnification view of region circled in (a), with red arrows pointing at α-Fe(Mo) grains, yellow arrows at μ-Fe_3Mo_2 and/or Fe_3Mo_3C Mo-rich grains, and green arrow at needle-shaped region; (d) Fe elemental EDS map; (e) Mo EDS elemental map.

% (41.7 vol%). The remaining is divided between μ-Fe_3Mo_2 (45.1 mol% or 38.1 vol%) and Fe_3Mo_3C (3.4 mol% or 20.1 vol%). The carbide phase is expected to form during the reduction and sintering steps *via* reaction of carbon remaining in the foam after the binder burnout. Bulk chemical analysis confirms the presence of carbon in the foams at a level of 0.49 wt%, consistent with the phase fractions presented above.

Within the microstructure visible in the SEM micrographs (Fig. 2c), these phases are apparent as two distinct micron-size regions (expected to be single grains), distinguishable by variations in contrast in the backscattered SEM micrograph: Fe-rich (Fig. 2c red arrows, Fig. 2d) and Mo-rich (Fig. 2c yellow arrows, Fig. 2e). The latter region may consist of μ-Fe_3Mo_2 and/or Fe_3Mo_3C which are indistinguishable due to similar average Z values. In larger sintered volumes (Fig. 2c, dashed line), typically 5-10 μm in diameter, interfaces between α-Fe(Mo) + (μ-Fe_3Mo_2/ Fe_3Mo_3C) grains are visible, which is consistent with the Fe-Mo phase diagram (without C) at the sintering temperature, where α-Fe (with Mo in solid solution) exists in equilibrium with the μ-phase (Figure S2, blue line) [40,41]. The three-phase composition can be expected to contribute significantly to the sintering inhibition, as the distinct phases limit diffusion across the entire lamellae, unlike single-phase Fe, Fe-Ni and Fe-Co foams previously studied. The needle-like regions (Figure 1c) are found to be Mo-rich, as highlighted by green arrows in Fig. 2a and c, and thus are most likely μ-Fe_3Mo_2, given the rhombohedral crystal structure of the μ-phase.

3.2. Chemical evolution of foams during redox cycling

3.2.1. Oxidation evolution study via operando XRD

Chemical and crystallographic changes upon redox cycling of Fe-25Mo foams are studied *via operando* XRD, revealing phases present (diffraction peaks), reaction kinetics (change in peak intensity), and evolution in chemical composition of solid-solution phases (peak position shifts). The acquisition time was increased from 12 to 60 s, as compared to previous *operando* work on Fe, Fe-Ni, Fe-Co, and Fe-Cu [15, 30,31]; the five-fold longer exposure time was necessary to resolve peaks, due to increased absorption from high-Z Mo. To slow reactions rates in the small sample and resolve phase changes with longer, 1-minute scans, Ar was flowed through a 40 °C water bubbler (H_2O partial pressure: 0.073 atm, compared to 0.77 atm at 93 ºC) for oxidation, and a lower H_2 content (Ar-4% H_2) for reduction. Given these modifications, the present reaction kinetics for Fe-Mo foams, derived from *operando* XRD, cannot be compared to previous *operando* experiments, nor bulk samples; interrupted bulk sample measurements using identical conditions to previous studies are presented later, to compare reaction kinetics between alloy systems.

The entire redox process is represented in Fig. 3a, for a limited 2θ range containing the most intense reflections of each phase, whose integrated areas are shown in Fig. 3b–d. The initial phase composition is the same as the ex-situ XRD pattern for the as-sintered samples (Fig. 2b):

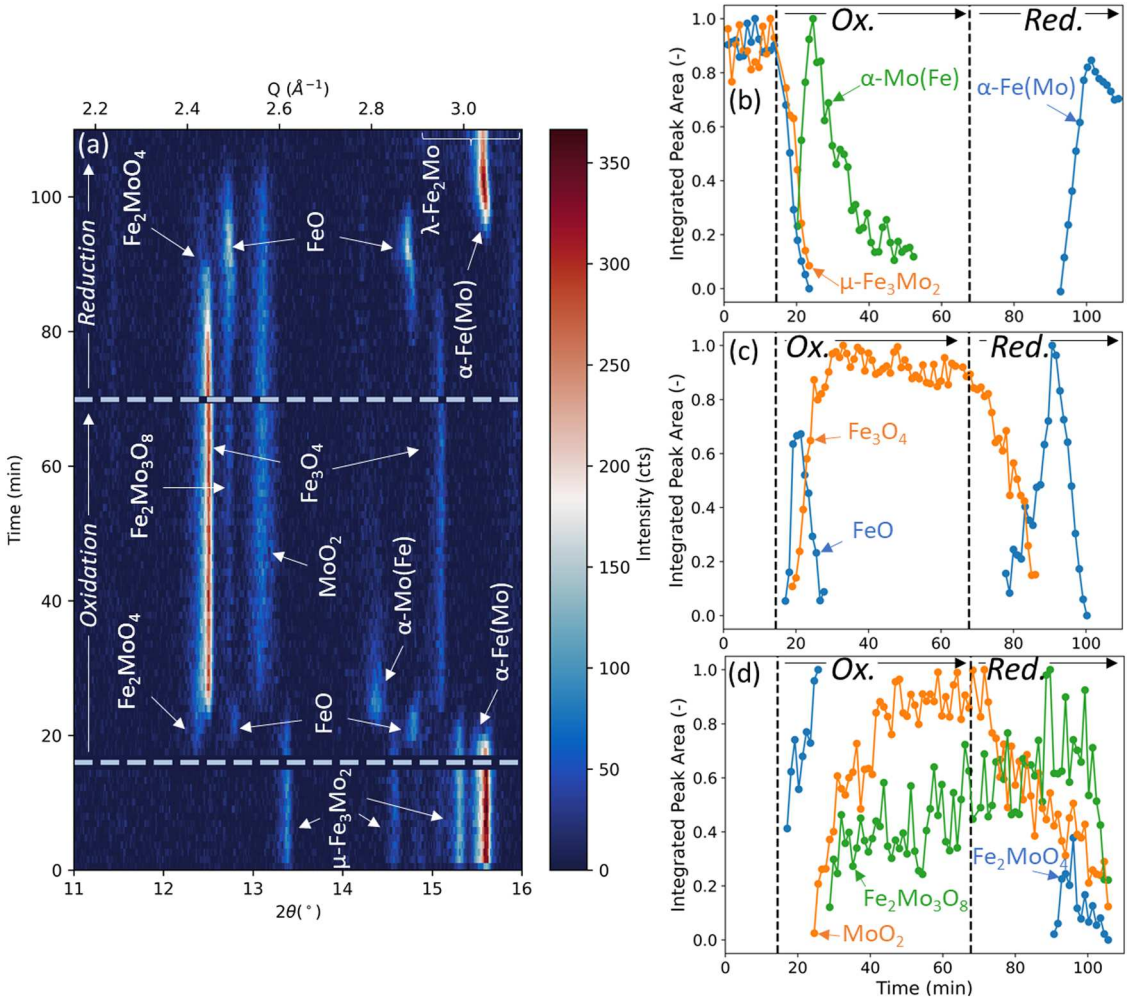

Fig. 3. *In-situ* XRD data of Fe-25Mo foam during the first redox cycle at 800 ºC. (a) Stacked XRD diffractograms, with time on y axis, for the entire first redox cycle. (b–d) Normalized peak integral of each phase, tracked for the most intense reflection throughout the redox process, with time on x axis, separated into (b) metallic phases: α-Fe(Mo) <110>, μ-Fe_3Mo_2 <116>, and α-Mo(Fe) <110>; (c) iron oxides: FeO <200>, and Fe_3O_4 <131>; (d) Mo-containing oxides: Fe_2MoO_4 <113>, $Fe_2Mo_3O_8$ <112>, and MoO_2 <110>.

α-Fe(Mo) and μ-Fe_3Mo_2. Fe_3Mo_3C is not measured here due to peak overlap with μ-Fe_3Mo_2. The sample is kept under 4% H_2-Ar at 800 °C for the first 15 mins to ensure temperature equilibration; however, no significant λ-Fe_2Mo Laves phase is formed during this time, despite the presence of this phase in the Fe-Mo phase diagram at 800 °C, indicating a sluggish transformation from μ-Fe_3Mo_2 (stable at the sintering temperature of 1000 °C) to λ-Fe_2Mo (stable at the redox temperature of 800 °C), as shown in Figure S2 (blue and orange lines) [41]. At the onset of oxidation (t = 15 min), α-Fe(Mo) and μ-Fe_3Mo_2 are rapidly consumed, as shown by the decreasing peak integral in Fig. 3b (blue and orange). The full oxidation of these initial metallic phases occurs in the first 9 minutes of oxidation; concurrently, an α-Mo(Fe) peak grows indicating that metallic Mo is rejected from the nascent oxide (Fig. 3b, green). The first oxide phase that forms is the mixed oxide Fe_2MoO_4 (Fig. 3d, blue), the only oxide phase in equilibrium with both α-Fe(Mo) and μ-Fe_3Mo_2, and the lowest oxidation state for a mixed oxide in the Fe-Mo-O ternary phase diagram [42]. Thereafter, FeO is formed at t = 17 min (Fig. 3c, green line), reaching a maximum at t = 19 min, at which time Fe_3O_4 begins forming (Fig. 3c, orange). The FeO lattice parameter shift, while not reported here, is consistent with our previous *in-situ* studies, indicating an O enrichment from the initially O-poor wüstite [30]. FeO is completely transformed to Fe_3O_4 at t = 26 min, 11 mins after the beginning of the oxidation period. This oxidation sequence (Fe→FeO→Fe_3O_4) is also observed in pure Fe foams [31]. At t = 25 min, metallic α-Mo(Fe) begins to oxidize, forming MoO_2. At roughly the same time, $Fe_2Mo_3O_8$ begins to form. The decrease of the initial mixed oxide, Fe_2MoO_4, corresponding to its further oxidation, is not tracked here, due to overlap with the Fe_3O_4 peak. Metallic α-Mo(Fe) is fully oxidized by t = 53 min, representing the last step of oxidation. The preferential oxidation of Fe seen here is kinetically driven, as MoO_2 is more stable than Fe_3O_4 at 800 °C [43].

3.2.2. *Fully oxidized composition and bulk oxidation kinetics*

When fully oxidized at the end of the first half cycle, the foam contains Fe_3O_4 (51.6 mol%, 60.7 vol%), MoO_2 (40.4 mol%, 21 vol%), and $Fe_2Mo_3O_8$ (8 mol%, 18.4 vol%) (Fig. 4a). Trace amounts of volatile MoO_3 are formed, as evidenced by condensation in the furnace tube, downstream of the sample; however, the amount formed is negligible, as no measurable mass loss is observed over 50 cycles of oxidation (<1 mg). This is consistent with previous studies of high-temperature steam oxidation of Mo [44]. Further, Fe_2O_3 is not seen, in agreement with previously-studied Fe foams and as expected from the inability to form Fe_2O_3 under steam [27], and no other mixed oxides present on the ternary Fe-Mo-O phase diagram are observed [42]. The fate of the carbon, initially combined in the Fe_3Mo_3C phase, is described in Figure S3. As Fe is preferentially oxidized over Mo, the binary Mo_2C forms after 10 minutes of oxidation. Utilizing a longer first oxidation half-cycle, this compound is fully oxidized after 2 h, eliminating all carbon from the foam (*via* formation of CO+CO_2), as there is little to no solubility of carbon in the oxide phases present. This is confirmed *via* chemical analysis, showing a low carbon content (0.025 wt%) after the first oxidation of the Fe-Mo foam, comparable to low C concentrations previously reported in Fe and Fe-Ni foams [31].

The full oxidation of the Fe-25Mo foam results in a theoretical mass gain of 0.36 g oxygen per gram of Fe-25Mo alloy, slightly lower than for pure Fe (0.38 g O / g). This is significantly higher than previously

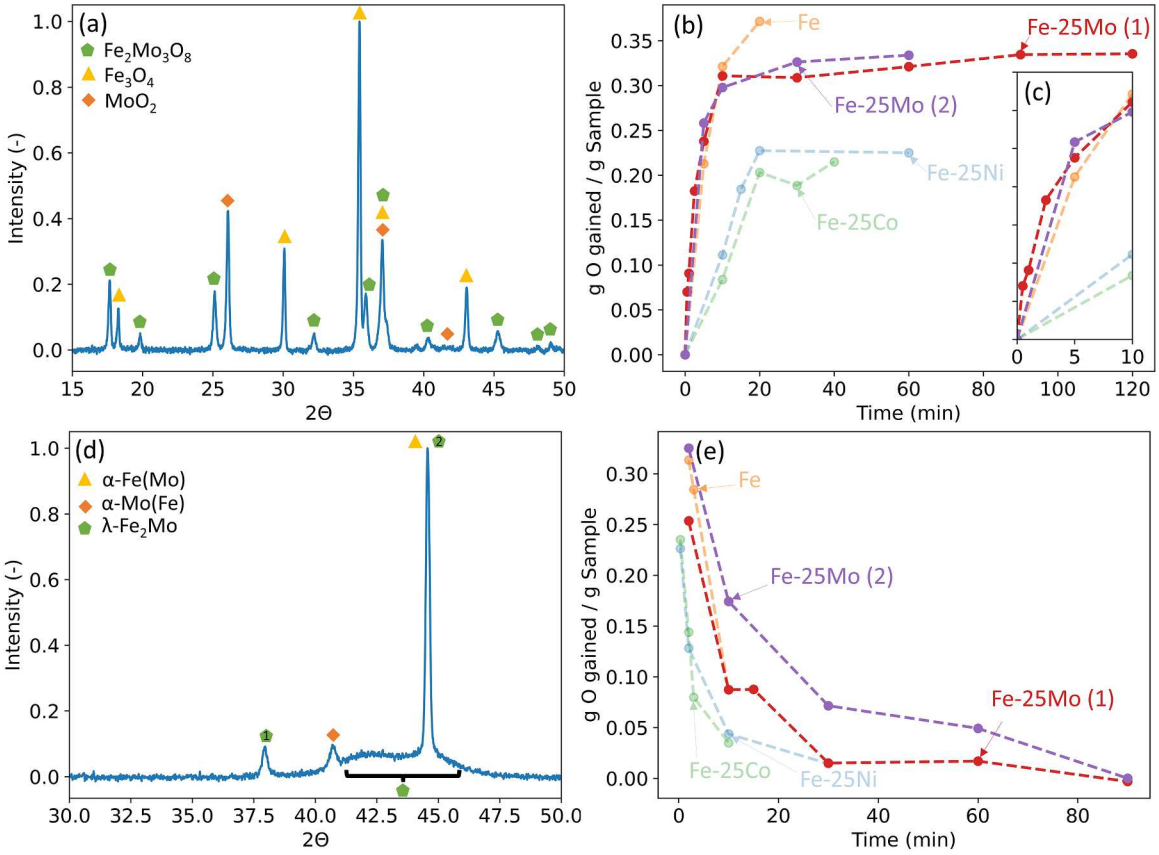

Fig. 4. (a) XRD pattern for fully oxidized Fe-25Mo foam after first oxidation half-cycle at 800 °C (measured *ex-situ* at 25 °C). (b) Specific mass gain as a function of oxidation time at 800 °C, for bulk Fe-25Mo foams (each data point, measured at 25 °C, represents a unique specimen). (c) Detailed view of (b) from 0–10 min, highlighting differences in early oxidation kinetics. (d) XRD pattern for fully reduced Fe-25Mo foam after 1 cycle at 800 °C (measured *ex-situ* at 25 °C). Green peaks 1 and 2 represent the (110) and (112) reflections for λ-Fe_2Mo, respectively. (e) Mass loss as a function of reduction time at 800 °C, for bulk Fe-25Mo foams (each data point, measured at 25 °C, represents a unique specimen). Fe-25Mo(1) and Fe-25Mo(2) curves refer to first and second oxidation half-cycles, respectively. Data for Fe, Fe-25Ni, and Fe-25Co foams are reproduced from Refs. [30,31].

studied Fe-25Ni and Fe-25Co (~0.28 g O / g) for which Ni and Co do not oxidize, unlike Mo. The time evolution of mass gain of Fe-25Mo foams during oxidation is shown in Fig. 4b, where the last point for each composition indicates full oxidation. The fully oxidized masses are somewhat lower than the above theoretical value, because of slight spallation of the oxide during foam handling. As compared to prior Fe-25Co or Fe-25Ni foams, the Fe-25Mo foams offer significantly faster initial oxidation during both the first and second cycles, equal or slightly faster than those shown by pure Fe foams (Fig. 4c). The ability of Mo to catalyze the oxidation of Fe has previously been explored [22,26,27]; however, the similar oxidation rate between Fe and Fe-25Mo seen here is likely a combination of the catalytic properties of Mo, the rate limiting Mo-oxidation step, and microstructural (porosity) effects, the latter of which is explored later. The rate of Fe-25Mo oxidation also increases after the first cycle; this is partly due to the lack of C in the second cycle, but also to microstructural changes after the first cycle. While, for the first ~ 10 min, the rate of O gain is slightly faster for Fe-25Mo foams as compared to Fe, the time to full oxidation for Fe-25Mo foams is longer than for pure Fe, and similar to that for Fe-25Co or Fe-25Ni foams (~ 60 min), reflecting the effect of the rate-limiting step of the Mo oxidation, which is responsible for the later mass gain in the Fe-25Mo foams.

3.2.3. Reduction evolution study via operando XRD

At t = 70 min, reduction is initiated as Ar-4% H_2 is introduced in the system (Fig. 3a). Due to the dilute amount of H_2 present in the reducing gas, there is a slight delay in the start of reduction, as the remaining steam from oxidation maintains an oxidizing environment. At t = 73 min, both Fe_3O_4 and MoO_2 begin reducing (Fig. 3c, d orange lines). Fe_3O_4 is first reduced to FeO (Fig. 3c, blue line), followed by a shift in lattice parameter to form O-deficient $FeO_{1.03}$ (Fig. 3a), and finally to α-Fe (Fig. 3b, blue line), consistent with the reduction of Fe_3O_4 to Fe observed in pure Fe foams [31]. Fe_3O_4 is fully reduced by t = 85 min, and FeO by t = 101 min. During that time, the majority of the MoO_2 is reduced directly to Mo, which then alloys with reduced α-Fe to form α-Fe (Mo). There is also a small amount of α-Mo(Fe) present after full reduction (Fig. 4d), although the corresponding diffraction peaks cannot be resolved in Fig. 3a. The MoO_2 reduction occurs over the entire 33 min reduction period, until t = 106 min, showing sluggish kinetics compared to those of Fe_3O_4 (28 min). During the MoO_2 reduction, a shift of the α-Fe(Mo) peak (Fig. 3a) is observed, consistent with dissolution of Mo in α-Fe, up to the 3 at% solubility limit at 800 °C [41]. While both MoO_2 and Fe_3O_4 are reduced, the peak integral of the ternary oxide ($Fe_2Mo_3O_8$) continues to increase (Fig. 3d, green line), as further discussed in Section 3.3.2. At t = 90 min, the $Fe_2Mo_3O_8$ peak begins to drop, coinciding with the slight formation of the mixed oxide, Fe_2MoO_4 (Fig. 3d, blue line). This phase is then also reduced within 16 min. The entire foam is fully reduced by t = 106 min, after 33 min of reduction. The phase evolution for the entire redox process is the same for subsequent cycles, as seen in *operando* data for the second redox cycle (Fig. S4).

3.2.4. Fully reduced composition and bulk reduction kinetics

After the first redox cycle, the foams initial phase composition after reduction and sintering (α-Fe(Mo) + μ-Fe_3Mo_2) is not recovered; instead, the foam contains α-Fe(Mo) (29.9 mol%, 28.5 vol%), λ-Fe_2Mo (69.0 mol%, 69.9 vol%), and small amounts of α-Mo(Fe) (1.1 mol%, 1.6 vol%), as illustrated in the x-ray spectrum shown in Fig. 4d. In this spectrum, the λ-Fe_2Mo phase contributes a broad shoulder (2θ ~ 41–46°) consistent with a nanocrystalline state, and two distinct peaks: <1 1 0> (2θ– 38°), and <1 1 2> (2θ ~ 44.5°). The nanocrystalline form of Fe_2Mo has been previously reported after H_2 reduction of mixed Fe-Mo oxides, primarily Fe_2MoO_4, similar to the reaction studied here [40]. Morales *et al.* predict a single-step reaction, $Fe_2MoO_4 + 4\ H_2 \rightarrow Fe_2Mo + 4\ H_2O$, implying that λ-$Fe_2Mo$ forms near the end of the reduction of our foam, after dissolution of reduced Mo into α-Fe(Mo) [40]. The change in final composition - from α-Fe(Mo) + μ-Fe_3Mo_2 after reduction and sintering to α-Fe(Mo) + λ-Fe_2Mo after the first redox cycle - can be attributed to changes in operating temperature, as sintering occurs at 1000°C and redox cycling at 800 °C. The new α-Fe(Mo) + λ-Fe_2Mo composition is consistent with experimental phase diagrams [41], and is also observed after each subsequent cycle.

As shown in Fig. 4e, when reduction initiates, the rate of mass loss for the Fe-25Mo and pure Fe foams are initially similar. At longer times, the rate for Fe-25Mo slows, due to the rate-limiting Mo-oxide reduction. The reduction rate is also significantly slower than those of previously-studied Fe-25Ni and Fe-25Co foams, where metallic Ni and Co catalyze the reduction of Fe-oxide [30,31], implying that the Mo-oxide does not have a similar catalytic effect. To ensure full reduction of Fe-25Mo foams, a 90-minute reduction half-cycle is thus needed. Also, the reduction rate of the Fe-25Mo foam on the second cycle is slower than that of the first cycle (Fig. 4e, purple and red lines); since the chemical reaction is the same during reduction, one possible explanation is microstructural changes, which are discussed in detail in Section 3.3.

3.3. Microstructural evolution of lamellae

Based on the above understanding of the chemical evolution of both Fe and Mo during redox cycling of our Fe-25Mo foams, the microstructural evolution can be explored and compared with those of both unalloyed Fe and alloyed Fe-25Ni, and Fe-25Co foams previously studied. In the experiments described below, Fe-25Mo foams were cycled at 800°C, and long half-cycle times were utilized to ensure full oxidation and reduction (analog to full charge and discharge) and study the microstructural changes relevant for the complete reactions.

3.3.1. Oxidation

The microstructural evolution of the Fe-25Mo lamellae during oxidation is illustrated in Fig. 5. In samples with low levels of oxidation, ion-milling was performed after polishing, revealing significant internal microporosity, which appears discrete and closed, within sintered regions of the lamellae (Fig. 5a,b blue arrows). Microchannels likely form within the lamellae during the original reduction and sintering process, where incoming H_2 reacts with the oxides, releasing steam, and preventing sintering in these regions. This creates a network of steam-egress microchannels within each lamella; combined with the sintering inhibition of Mo, many of these channels are still present after the 3.5 h of sintering following the reduction step. The same phenomenon was previous reported in Fe-based foams, but some of the microchannels coalesced and partially sintered, limiting gas access to the interior of the lamellae [30,31].

Oxidation initiates at the surface of each grain on the internal surface of steam-egress channels (Fig. 5b, O map and red arrows). Given the surface reactivity, the increased oxidation rate seen in Fig. 5b for Fe-25Mo, as compared to prior Fe, Fe-25Ni and Fe-25Co foams, is likely due to the increased surface-to-volume ratio of the microporous lamellae. Early during oxidation, most of the lamellar solid matrix is separated into Fe-rich and Mo-rich regions, assumed to be individual grains (Fig. 5b, Fe and Mo maps). As oxidation proceeds, the volumetric expansion of the Fe and Mo oxides fills the microporosity and steam-egress microchannels within the partially sintered lamellae, where the expansion to Fe_3O_4, MoO_2, and $Fe_2Mo_3O_8$ is between 109.8 – 111.9%. Reaching full oxidation, only a few small pores are left within the mostly dense oxide lamellae (Fig. 5c). Lamellar external surfaces, seen in Figure S5, also appear almost fully dense, with a highly faceted surface and few open surface pores. Kirkendall porosity, which occurs extensively in unalloyed Fe foams [16], is significantly limited in the Fe-25Mo foams due to two primary factors: (i) interlamellar porosity between solid regions and as steam-egress microchannels reduce the diffusion distance for Fe and Mo moving out and for O moving in, forming fewer Kirkendall pores; and (ii) the gas-egress channels, combined with plastic deformation in the oxides [29] initially act as Kirkendall pore sinks, further decreasing the presence of these pores.

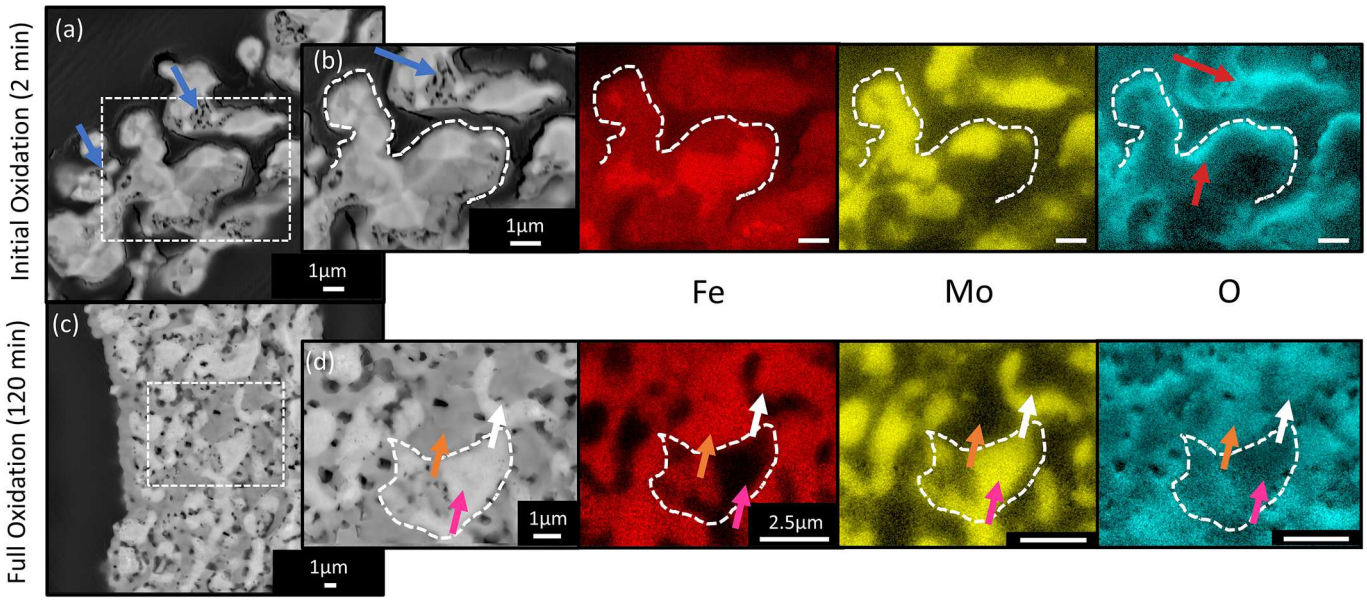

Fig. 5. Microstructure of Fe-25Mo lamellae early and late during the first oxidation half cycle at 800 °C, shown in radial cross sections under SEM-BSE imaging (grey), with corresponding EDS maps for Fe (red), Mo (yellow), and O (blue). (a, b) cross section after early oxidation (2 min), (c, d) cross section after full oxidation (120 min). Blue arrows highlight internal porosity revealed via ion-milling, red arrows show regions where oxidation has initiated, orange arrows show Fe-rich regions, magenta arrows Mo-rich regions, and white arrows regions rich in both Fe and Mo. Dotted lines outline regions to help comparing the EDS maps.

At full oxidation, two different regions are visible in the BSE cross-section; a darker Fe-rich region (Fig. 5d, orange arrows), and a brighter Mo-rich region (Fig. 5d, magenta arrows). The oxygen map appears darker in Mo-rich regions (Fig. 5d), which is due to the attenuation of signal from the Mo, compared to Fe, not to O depletion. $Fe_2Mo_3O_8$ and MoO_2 have similar average atomic mass, making them mostly indistinguishable in EDS maps. However, immediately surrounding the Mo-rich regions in Fig. 5d, there is a slight decrease in Mo intensity and a slight increase in Fe intensity, indicated by white arrows. This is consistent with ternary oxide regions present between Fe_3O_4 and MoO_2 and is further supported by the reduction pattern detailed in Section 3.3.2. The three oxides present at full oxidation - $Fe_2Mo_3O_8$, Fe_3O_4, and MoO_2 - have no solubility with each other, explaining the distinctly separated regions [42]. The fine, interpenetrating microstructure (Figure S5) of this multi-phase system prevents Fe_3O_4 sintering, reminiscent of the microstructure and outcome observed for ZrO_2-Fe_2O_3-Al_2O_3 mixtures prepared by solution precursors [45,46]. In these multi-phase ceramics, grain growth is inhibited by neighboring grains with a different composition and with limited solid solubility, suppressing long-range interdiffusion needed for sintering. A similar microstructure is presented here, maintaining for multiple cycles the fine, equiaxed grain size observed initially.

Despite the lack of a metallic core (which provides adhesion to the oxides in Fe-25Ni and Fe-25Co foams [30,31]), no lamellar splitting is

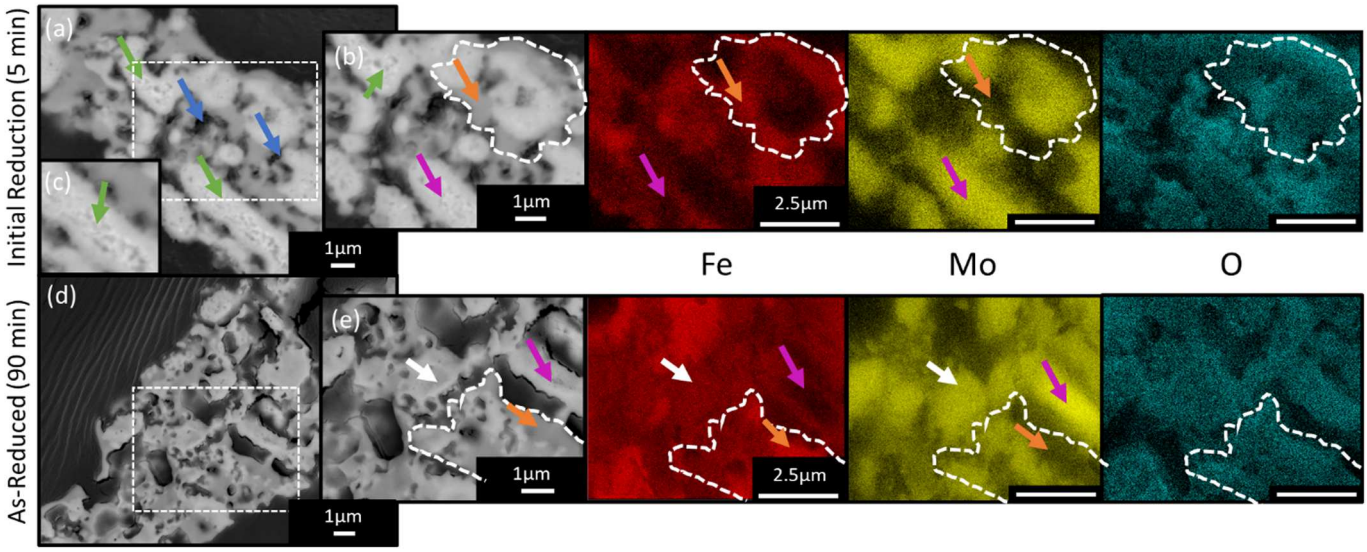

Fig. 6. Evolution of microstructure of Fe-25Mo lamellae early and late during the first reduction half cycle at 800 °C, shown in radial cross sections under SEM-BSE imaging (grey), with corresponding EDS maps for Fe (red), Mo (yellow), and O (blue). (a, b) cross section after 5 min of reduction, (c) magnified view of speckled region, (d, e) cross section after full oxidation (90 min). Blue arrows highlight internal porosity, green arrows point to speckled patterns within Mo-rich regions, orange arrows to Fe-rich regions, white arrows to mixed Fe-Mo regions, and magenta arrows to Mo-rich regions. Dotted lines outline regions to guide the eye in EDS maps.

observed in the Fe-25Mo lamellae when fully oxidized. Some fracture likely still occurs within these oxidized lamellae, however, due to the large volumetric expansion upon oxidation and the brittleness of the oxide. The presence of significant intra-lamellar microporosity might interrupt large-scale crack propagation, meaning that fracture is localized within smaller regions; also, as oxidation proceeds, leading to volumetric expansion, fractured regions are recontacted and may sinter together, thus possibly healing some of the cracks.

3.3.2. *Reduction*

Reduction initiates primarily at the interface between the Fe-rich and Mo-rich grains, where newly reduced Fe generates micropores due to the volumetric shrinkage (Fig. 6a, blue arrows). Within the Mo-rich regions (Fig. 6a, b, magenta arrows), a speckled pattern (Fig. 6a, b, green arrows) can be seen on the interior, highlighted in Fig. 6c. As Fe_3O_4 and MoO_2 begin reduction near simultaneously (Fig. 3), the speckled pattern is likely due to newly reduced Mo, creating pores due to volumetric shrinkage and contrast differences between oxide and metal. The speckled pattern is only present in the interior of the Mo-rich region, where mixed oxide surrounds the MoO_2, which provides the following scenario: as the MoO_2 central region is reduced, the outgoing steam contacts the surrounding mixed oxide, preventing it from reducing, consistent with the reduction pattern seen in the operando experiments. At this point in reduction, distinct metallic regions rich in Fe (Fig. 6b, orange arrows), and Mo (Fig. 6a, b, magenta arrows) still exist.

As reduction proceeds, more microporosity is created within the lamellae (Fig. 6d). Select regions of α-Mo(Fe) (Fig. 6e, magenta arrows) and α-Fe(Mo) (Fig. 6e, orange arrows) are visible in the fully reduced

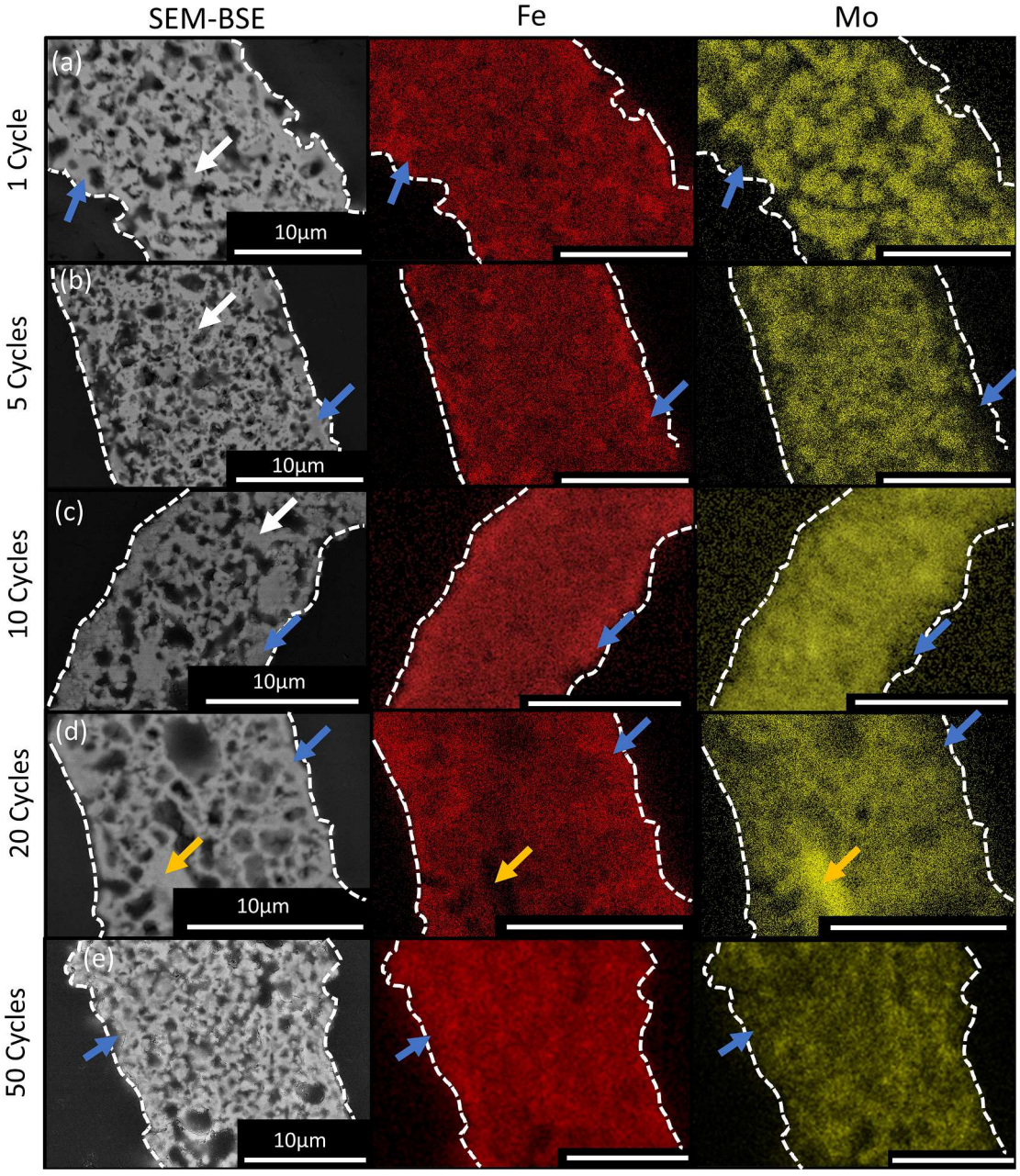

Fig. 7. Evolution of lamellar microstructure in Fe-25Mo foams after 1, 5, 10, 20 and 50 redox cycles at 800 °C, shown in radial cross sections under SEM-BSE imaging, with corresponding EDS maps for Fe (red) and Mo (yellow). Dotted lines outline regions to guide the eye. Blue arrows indicate Fe-enrichment in the outer surface of lamellae, white arrows indicate densified regions in the interior of the lamellae, and yellow arrows indicate Mo-enriched regions in the lamella interior.

microstructure. Much of the interior contains both Fe and Mo, forming grains of λ-Fe_2Mo (Fig. 6e, white arrows). The equilibrium between α-Fe (Mo) and λ-Fe_2Mo prevents full re-homogenization across the lamella, in contrast to what was previously observed in Fe-25Ni and Fe-25Co, both of which exhibit wide solid solutions [30,31]. Lamellae, after the first cycle, still show porosity open to the surface (Fig. S6a). However, the needle-like regions seen in the as-sintered lamellae no longer exist, replaced by large smooth surfaces (Fig. S6b), likely α-Fe(Mo) or α-Mo (Fe). Open surface porosity, highlighted in Fig. S6c, reveals a highly porous interior, with a morphology consistent with that of nano-crystalline λ-Fe_2Mo [47]. The high surface area within the lamellar interior is another reason that the oxidation rate may increase upon the second cycle, as seen in Fig. 4b.

3.4. Foam evolution over multiple cycles

With an understanding of the microstructural evolution over the first redox cycle, foams were subjected to multiple consecutive cycles at 800 °C to explore the stability of (i) the newly formed, porous microstructure, and (ii) the macrostructure of the foam. Given the high operating temperature and high extent of reaction, these cycles lead to accelerated degradation, with the primary goal of exposing underlying mechanisms. Two freeze-cast wavelengths (defined as the width of a lamella plus its adjacent channel) were tested: λ = 50 and 30 μm. The mechanisms observed did not vary based on wavelength. All results here refer to large-wavelength (λ = 50 μm) foams, small-wavelength results are available in Section S1 (Figs. S7 and S8).

3.4.1. Microstructural Evolution

The microstructural evolution of Fe-25Mo lamellae, up to 50 consecutive redox cycles, is illustrated in Fig. 7. After the first redox cycle, significant microporosity exists within the lamellae (Fig. 7a). The exterior of the lamellae is rich in Fe (Fig. 7a, blue arrows)), forming α-Fe (Mo), whereas the interior contains both Fe and Mo, indicating λ-Fe_2Mo is present. The exterior Fe-rich layer is reminiscent of the shell formation which is systematically found in unalloyed Fe foams and powder-beds; in unalloyed Fe foams repeated cycling causes flaring of the lamella tips, resulting in the formation and growth of a dense Fe shell that greatly slows the kinetics of further reaction by blocking the ingress of gas to the sample [20]. A similar deleterious gas-blocking Fe layer is formed in packed powder beds as well, as shown by Berger et al [11]. However, two differences are present that prevent the shell observed in the studied Fe-25Mo foams from drastically impacting reaction kinetics: (i) the sintering inhibition of Mo prevents the creation of a continuous shell at the lamellar surface, allowing gas access to the porous volume of the lamellae, and (ii) the shell is very thin (~1 μm wide) and is thus expected to crack when oxidized, providing additional gas flow to the lamellar interior.

For 5 redox cycles (Fig. 7b), the Fe enrichment on the lamellar surface is maintained, stemming from the preferential oxidation of Fe. This exterior Fe-rich layer, however, does not thicken over subsequent cycles; this implies that the lamellae have segregated into two distinct regions, where the exterior is Fe-3Mo, forming the most saturated solid solution α-Fe(Mo) following oxidation, and the interior is ~ Fe-33Mo, forming the nanocrystalline λ-Fe_2Mo. Grains, indicated by white arrows in Fig. 7, varies with cycles between individual lamellae, as the microporosity that defines the microstructural pattern of the lamella interior stems from volumetric shrinkage during reduction and therefore the path of gas flow access through the torturous steam-egress channels, which varies by location. The microporosity is stable for extensive redox cycling, as shown after 10 cycles (Fig. 7c), 20 cycles (Fig. 7d), and 50 cycles (Fig. 7e); this microstructural stability indicates that the sintering inhibition provided by Mo does not fade with cycling. At longer cycle times, Mo-rich grains can be found in the interior of the lamellae (Fig. 7d, yellow arrows). Overall, despite variability in grain morphology, depending on cycle and lamellae chosen, the functionality of supplying gas flow to the entire foam, allowing it to react rapidly, is maintained. After 50 cycles, coarsened regions with a spherical, bulb-like shape grow on the lamellae. These features, which are depicted and further discussed in Figure S9, may enhance lamellar sintering and reduce redox kinetics, but these effects remain relatively mild.

3.4.2. Macrostructural evolution

Fig. 8 shows low-magnification radial cross-sections of Fe-25Mo foams after 1, 5, 10, and 20 redox cycles. The foams exhibit well-aligned lamellae arranged in large colonies throughout most of the foam; misaligned colonies occasionally appear near the edge of the sample, likely stemming from lower suspension stability for Fe_2O_3-MoO_3 slurries and slight radial temperature gradients from the mold (Fig. 8a, orange arrows). After 5 redox cycles (Fig. 8b) and 10 redox cycles (Fig. 8c), lamellae remain flat and unbuckled, and do not contact each other. The periphery of the foams (blue arrows) is, in all previous Fe-, Fe-Ni and Fe-Co foam studies, the first region to densify into a shell that can encapsulate the foam, as lamellae tips fracture and contact each other [20]. No shell formation occurs for the Fe-25Mo foam after up to 10 redox cycles, indicating a significant structural improvement. While most lamellae appear unbuckled, some buckling is visible after 10 cycles (Fig. 8c, green arrows). Even though the porous lamellae in the present Fe-25Mo foam have more buckling resistance than dense lamellae in the previously studied Fe-25Ni/Co foams, buckling occurs over repeated volumetric expansion and contraction; this is likely due to the high lamellar aspect ratio (for the larger wavelength foam) and the boundaries between neighboring colonies, which prevent longitudinal lamellar expansion. These effects are somewhat mitigated for small-colony foams, as shown in Fig. S8.

These effects become more visible with additional cycles, seen after 20 cycles in Fig. 8d. The extent of buckling is largely influenced by colony orientation, and how colonies are constrained by neighboring colonies, as evidenced by variations in local buckling behavior (Fig. 8d, black and white arrows). Despite increased buckling after 20 cycles, lamellae still do not contact in either the bulk of the foam or at its periphery.

Redox cycling was continued up to 50 redox cycles, as shown in Fig. 9. The microtomographic reconstruction (Fig. 9a) reveals that channels between neighboring lamellae are largely retained, despite clearly visible buckling (Fig. 9a, blue arrows). However, there is significantly more contacting of neighboring lamellae (Fig. 9b, yellow arrows) and more pronounced buckling (Fig. 9b, blue arrows) than seen after 20 cycles. Despite contact between neighboring lamellae, however, the foam is still mostly oxidized within the 90-minute period. Some entrapped Mo content remains, as shown previously in Fig. 7d, e. Two mechanisms may explain the ability for the Fe-25Mo foam to maintain stable reaction rates even after interlamellar contact: (i) internal lamellar porosity allows sintered neighboring lamellae to still undergo redox reaction, as gas can reach into the lamellae to oxidize the material, instead of relying on bulk diffusion from the surface, and (ii) due to sintering inhibition provided by Mo, neighboring lamellae may sinter locally at discrete contact points, but without full merging and local densification, and without widespread outer shell formation, which leads to encapsulation, as previously observed in Fe, Fe-Ni and Fe-Co foams [30,31].

The channel volume fraction (reported here as channel porosity), channel width, and lamellar width of the Fe-25Mo foams (λ = 30 and 50 μm), as measured from optical micrograph cross sections (such as those displayed in Fig. 9), are compared in Fig. 10 with those of previous alloyed foams (Fe-25Ni and Fe-25Co) and unalloyed Fe foams. Channel porosity here refers to the pore space between lamella, and excludes porosity contained within lamella themselves. The higher initial channel porosity of the Fe-25Mo foams, provided by the sintering inhibition effect of Mo, is clearly visible in Fig. 10a. As foams undergo cycling, the channel porosity of the unalloyed Fe foam rapidly decreases from 63 to 31% over the first 5 cycles. This stems from Kirkendall porosity

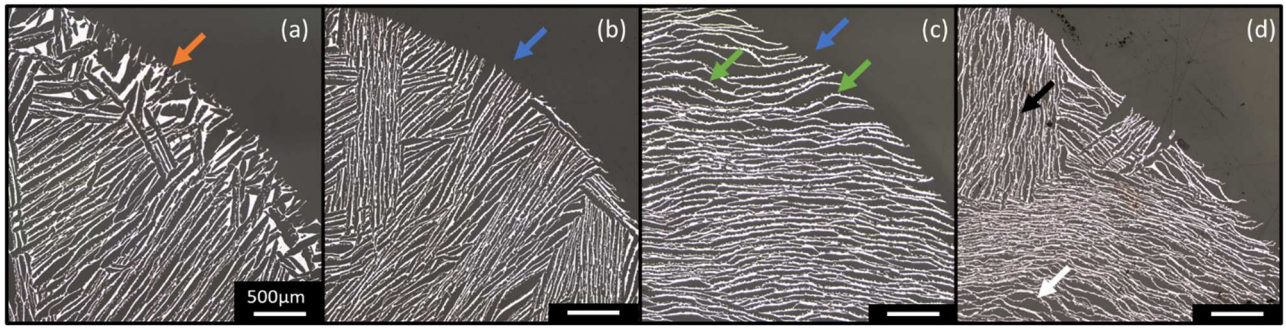

Fig. 8. Optical micrographs of radial cross sections for Fe-25Mo foams after (a) 1 cycle, (b) 5 cycles, (c) 10 cycles, and (d) 20 cycles at 800 °C. Orange arrow highlights misoriented colonies at foam edge (shown with blue arrows), and green arrows point to evidence of lamellar buckling (black and white arrows show contrasting levels of buckling).

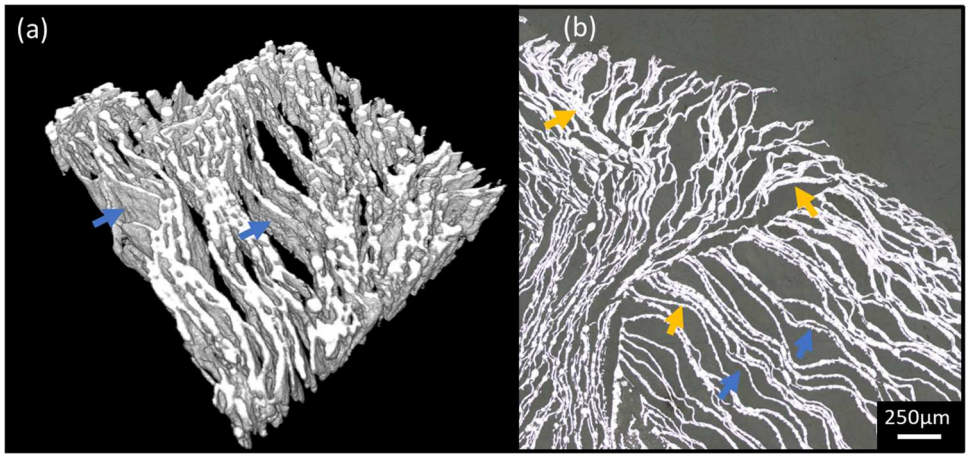

Fig. 9. Fe-25Mo foams after 50 consecutive redox cycles at 800 °C. (a) Tomographic reconstruction of Fe-25Mo foam, reconstructed volume is 180 μm in height. (b) Optical micrograph of radial cross section of foam. Blue arrows highlight examples of lamellar buckling, yellow arrows sintered regions.

formation and lamellar fracture, which lead to contacting and sintering of neighboring lamellae [16], as reflected by the increase in average lamellar thickness, up to 80 μm in Fig. 10b. The average channel thickness initially increases, as sintered lamellae create large channels; however, as foam densification continues, the channel thickness decreases (Fig. 10c). The channel porosity of Fe-25Ni and Fe-25Co is retained for longer times, but due to the onset of buckling, after 10 redox cycles, it decreases from ~73 to ~40%, with an increase in lamellar thickness (Fig. 10b). Variations in average channel width are detailed in previous work [30,31].

In contrast, the Fe-25Mo foams exhibit significantly better performance during redox cycling. Channel porosity is largely constant throughout the first 10 cycles, within 3% of the reduced+sintered value. This is reflective of both higher lamellar buckling resistance and increased sintering inhibition, as discussed above. Further, the lamellar thickness and channel width are near constant over the first 10 cycles, indicating little to no buckling or lamellae sintering. Beyond 10 cycles, there is a slight decrease in channel porosity (for the larger wavelength foam, dropping from 73 to 66% after 50 cycles), and an associated increase in both lamellar thickness and channel width, stemming from buckling and the formation of bulb-shaped coarsened region (described in Section S2 and Figure S9). Despite a five-fold increase in cycle number, however, the larger wavelength Fe-25Mo foam has much higher channel porosity, and significantly more stable channel width and lamellar thickness, than previously studied Fe, Fe-25Ni and Fe-25Co foams. The small-wavelength Fe-25Mo foam exhibits an even higher level of stability, due to better buckling resistance of lower aspect-ratio lamellae [31]. These results compare favorably with recent improvements to packed powder bed systems as well: Eigen, Rutjens, and Schroeder recently presented a study of Fe-Ni-YSZ composite powders undergoing similar redox cycling conditions with stable porosity of 68% up to 104 cycles for a composition of equimolar Fe_2NiO_4 and YSZ [48]. The Fe-25Mo foams presented here achieve a similar or higher level of porosity retention, but without the addition of inert phases that reduce the specific capacity of the material. Overall, both Fe-25Mo foams show remarkable structural improvements compared to previously studied Fe, Fe-25Ni and Fe-25Co foams, and they exhibit highly porous, lamellar structures after >125 h of continuous redox cycling at 800 °C.

4. Conclusions

Freeze-cast Fe-25Mo (at%) lamellar foams, when subjected to steam-hydrogen redox cycling at 800 °C, are much more damage- and sintering-resistant than previously-studied Fe, Fe-25Ni and Fe-25Co foams. Molybdenum alloying provide high macro- and microstructural stability, as well as high reaction reversibility: after 50 redox cycles at 800 °C, Fe-25Mo foams maintain 65% open porosity (i.e., ~80% of their initial porosity).

The high structural damage resistance of Fe-25Mo foams stems from the sintering inhibition behavior of Mo, creating a hierarchically porous foam. The porous hierarchy consists of wide channels between neighboring lamellae, and microporosity within each lamella. The wide channels provide easy gas access to the entirety of the foam and enable gas flow with no tortuosity; the wide channels also prevent contact between neighboring lamella due to expansion during oxidation. These

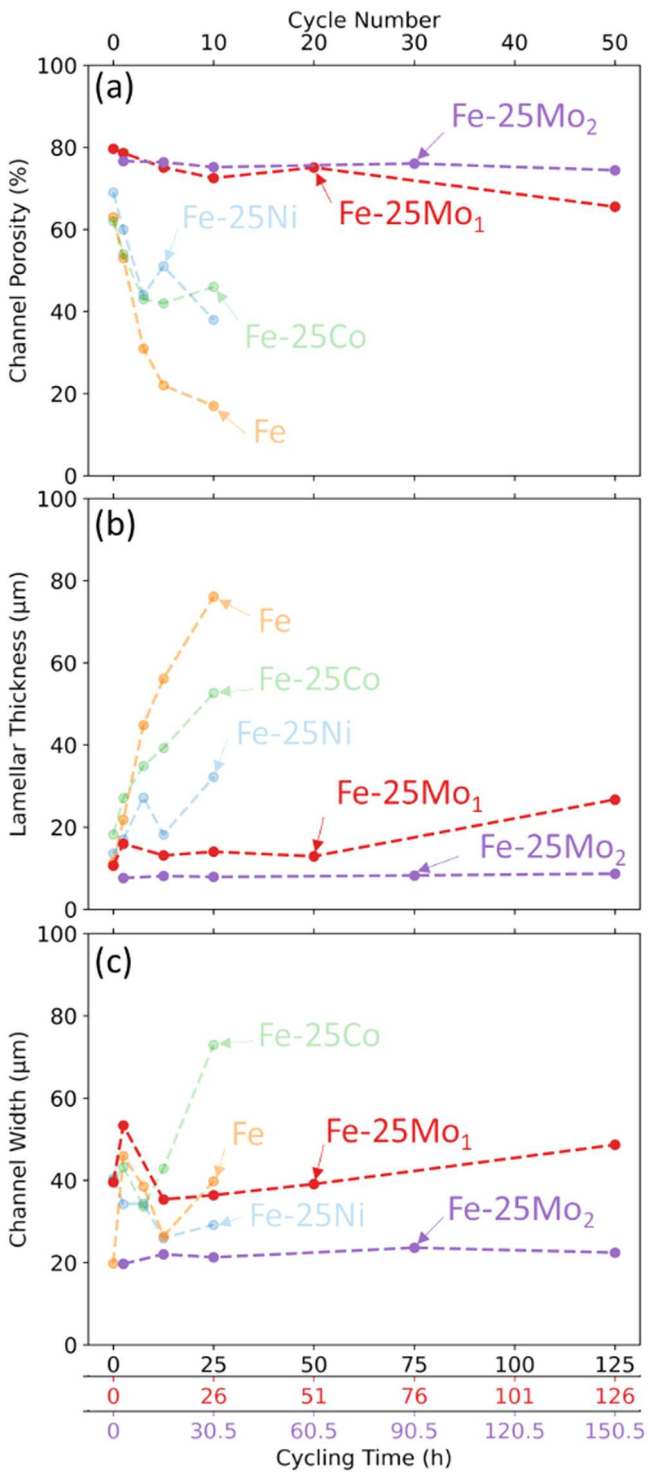

Fig. 10. Evolution with respect to redox cycle number (and cycling time) at 800 °C of (a) channel porosity (i.e., channel volume fraction), (b) mean lamellar thickness, and (c) mean channel width. Fe-25Mo$_1$ refers to lamellar wavelength $\lambda = 50$ μm, Fe-25Mo$_2$ refers to $\lambda = 30$ μm. Data for Fe, Fe-25Ni, and Fe-25Co foams are reproduced from Refs. [30,31]. Black x-axis represents cycle times for Fe, Fe-25Ni, and Fe-25Co foams, red and purple x-axis represent cycle times for Fe-25Mo$_1$ and Fe-25Mo$_2$ foams, respectively. Each data point represents an individual sample.

features are not, however, distinct to Fe-25Mo foams and were previously shown to be insufficient to prevent degradation during redox cycling. The micropores, therefore, provide a key second level of stability: they further increase gas access and lower the diffusion distance to the reaction front, accelerating both oxidation and reduction, they accommodate volume expansion locally, lowering mechanical stresses within each lamella, and they act as Kirkendall pore sinks, preventing the formation of deleterious closed porosity.

The hierarchically porous structure described above alone is not sufficient to enable long-term reversibility: similar hierarchical porosity observed in the Fe-25Ni and Fe-25Co system was observed initially, but the lower level of porosity disappears with continued cycling. The Fe-25Mo system, however, maintains both levels due to the redox activity and sintering inhibition of Mo and its oxides. Unlike Ni and Co, Mo is oxidized by steam. This allows a multi-phase oxide foam to form during oxidation, consisting of Fe_3O_4, MoO_2, and $Fe_2Mo_3O_8$. The interpenetrating nature of this foam prevents the coarsening of Fe_3O_4 in each lamella, thus preserving the hierarchical porosity inherent in the foam. Conveniently, the oxidation kinetics of Fe are enhanced in the presence of Mo, though this is somewhat offset by the comparatively sluggish kinetics of formation and reduction for MoO_2 and $Fe_2Mo_3O_8$. The complete formation of these oxides is important however, as it is through their reduction that the nanocrystalline phase λ-Fe_2Mo can form. The morphology of this phase further hastens subsequent oxidation, further improving performance during long term cycling.

While these properties have been shown to greatly improve anode resistance to degradation during the reactions performed herein, the results of this study must be considered in the context of reactions performed far from equilibrium, as the flowing gas consists entirely of either H_2O or H_2. In this way, the results are expected to closely resemble those found in chemical looping combustion reactors, but may be different than those found in iron-air batteries, where the gas mixture contains both H_2O and H_2. The properties that enable long-term stability will still be found in a current-drawing device, but the consequences for kinetics and voltammetry remain to be studied.

Data and materials availability

All data needed to evaluate the conclusions in the paper are present in the paper and/or the Supplementary Materials.

CRediT authorship contribution statement

Jacob B. Mack: Conceptualization, Investigation, Data curation, Visualization, Writing – original draft. **Samuel M. Pennell:** Conceptualization, Investigation, Visualization, Writing – review & editing. **David C. Dunand:** Conceptualization, Writing – review & editing, Funding acquisition.

Declaration of Competing Interest

The authors declare the following financial interests/personal relationships which may be considered as potential competing interests: DCD discloses a financial interest in Cell Mobility, Inc., which is commercializing freeze-cast metal foams.

Acknowledgments

The authors acknowledge Dr. Christos Malliakas (NU) for assistance with XRD experiments, Dr. William Guise (APS) in collecting tomographic data and Dr. Denis Keane (APS) in reconstructing tomographic data.

Funding

This research was funded by the US National Science Foundation

under grant CMMI-2015641. Experiments and characterization made use of the Materials Characterization and Imaging Facility, the NUANCE Center (supported by SHyNE under NSF ECCS-1542205, MRSEC under NSF DMR-1720139, the International Institute for Nanotechnology, the Keck Foundation, and the State of Illinois), and the IMSERC X-Ray facility (supported by SHyNE under NSF ECCS-2025633) at Northwestern University (NU). Microtomography was performed at the DuPont-Northwestern-Dow Collaborative Access Team (DND-CAT) located at Sector 5 of the Advanced Photon Source (APS). DND-CAT is supported by Northwestern University, The Dow Chemical Company, and DuPont de Nemours, Inc. This research used resources of the Advanced Photon Source, a U.S. Department of Energy (DOE) Office of Science User Facility operated for the DOE Office of Science by Argonne National Laboratory under Contract No. DE-AC02-06CH11357.

Supplementary materials

Supplementary material associated with this article can be found, in the online version, at doi:10.1016/j.actamat.2023.119015.

References

[1] W. Drenckhahn, et al., A novel high temperature metal-air battery, Electrochem. Soc. 50 (2013) 125–135.
[2] C. Zhang, K. Huang, A comprehensive review on the development of solid–state metal–air batteries operated on oxide–ion chemistry, Adv. Energy Mater. 11 (2020).
[3] C. Wang, et al., Recent progress of metal–air batteries—a mini review, Appl. Sci. 9 (2019) 2787.
[4] A. Dinesh, et al., Iron-based flow batteries to store renewable energies, Environ. Chem. Lett. 16 (2018) 683–694.
[5] S. Bock, M. Pauritsch, S. Lux, V. Hacker, Natural iron ores for large-scale thermochemical hydrogen and energy storage, Energy Convers. Manag. 267 (2022), 115834.
[6] S. Trocino, M. Lo Faro, S.C. Zignani, V. Antonucci, A.S. Aricò, High performance solid-state iron-air rechargeable ceramic battery operating at intermediate temperatures (500–650 °C), Appl. Energy 233–234 (2019) 386–394.
[7] C. Zhang, K. Huang, An intermediate-temperature solid oxide iron–air redox battery operated on O2–-chemistry and loaded with Pd-catalyzed iron-based energy storage material, ACS Energy Lett. 1 (2016) 1206–1211.
[8] H. Ohmori, H. Iwai, Simulation of solid oxide iron-air battery: effects of heat and mass transfer on charge/discharge characteristics, J. Power Sources 286 (2015) 264–275.
[9] X. Zhao, X. Li, Y. Gong, K Huang, Enhanced reversibility and durability of a solid oxide Fe–air redox battery by carbothermic reaction derived energy storage materials, Chem. Commun. 50 (2013) 623–625.
[10] Y. Saito, F. Kosaka, N. Kikuchi, H. Hatano, J Otomo, Evaluation of microstructural changes and performance degradation in iron-based oxygen carriers during redox cycling for chemical looping systems with image analysis, Ind. Eng. Chem. Res. 57 (2018) 5529–5538.
[11] C.M. Berger, et al., Development of storage materials for high-temperature rechargeable oxide batteries, J. Energy Storage 1 (2015) 54–64.
[12] L. Huber, B. Gamisch, B. Dawoud, Experimental investigation of the cycle stability of different iron oxide composites for a redox hydrogen storage process, in: Proceedings of the International Renewable Energy Storage Conference 2021 (IRES 2021) 8, 2022, pp. 126–135.
[13] M.A. Shahbazi, M. Ghalkhani, H. Maleki, Directional freeze-casting: a bioinspired method to assemble multifunctional aligned porous structures for advanced applications, Adv. Eng. Mater. 22 (2020).
[14] L. Wu, Y. Li, Z. Fu, B.L. Su, Hierarchically structured porous materials: synthesis strategies and applications in energy storage, Natl. Sci. Rev. 7 (2020) 1667–1701.
[15] S.K. Wilke, D.C Dunand, Structural evolution of directionally freeze-cast iron foams during oxidation/reduction cycles, Acta Mater. 162 (2019) 90–102.
[16] S.K. Wilke, D.C. Dunand, In operando tomography reveals degradation mechanisms in lamellar iron foams during redox cycling at 800°C, J. Power Sources 448 (2020), 227463.
[17] H. Larsson, T. Jonsson, R. Naraghi, Y. Gong, R.C. Reed, J. Ågren, Oxidation of iron at 600 °C – experiments and simulations, Mater. Corrosion 68 (2017) 133–142.
[18] Y. Ma, et al., Hierarchical nature of hydrogen-based direct reduction of iron oxides, Scr. Mater. 213 (2022), 114571.
[19] S.H. Kim, et al., Influence of microstructure and atomic-scale chemistry on the direct reduction of iron ore with hydrogen at 700°C, Acta Mater. 212 (2021), 116933.
[20] S.K. Wilke, D.C Dunand, Finite element model for coupled diffusion and elastoplastic deformation during high-temperature oxidation of Fe to FeO, J. Electrochem. Soc. 167 (2020), 080532.
[21] C. Zhang, K. Huang, C. Zhang, K Huang, A comprehensive review on the development of solid-state metal–air batteries operated on oxide-ion chemistry, Adv. Energy Mater. 11 (2021), 2000630.
[22] K. Otsuka, T. Kaburagi, C. Yamada, S Takenaka, Chemical storage of hydrogen by modified iron oxides, J. Power Sources 122 (2003) 111–121.
[23] B. de Caprariis, M. Damizia, P. De Filippis, M.P. Bracciale, The role of Al2O3, MgO and CeO2 addition on steam iron process stability to produce pure and renewable hydrogen, Int. J. Hydrog. Energy 46 (2021) 39067–39078.
[24] E. Romero, R. Soto, P. Durán, J. Herguido, J.A. Peña, Molybdenum addition to modified iron oxides for improving hydrogen separation in fixed bed by redox processes, Int. J. Hydrog. Energy 37 (2012) 6978–6984.
[25] W. Wei, P.B. Samuelsson, A. Tilliander, R. Gyllenram, P.G. Jönsson, Energy consumption and greenhouse gas emissions during ferromolybdenum production, J. Sustain. Metall. 6 (2020) 103–112.
[26] H. Wang, J. Zhang, F. Wen, J. Bai, Effect of Mo dopants on improving hydrogen production by redox of iron oxide: catalytic role of Mo cation and kinetic study, RSC Adv. 3 (2013) 10341–10348.
[27] X. Liu, H. Wang, Hydrogen production from water decomposition by redox of Fe2O3 modified with single- or double-metal additives, J. Solid State Chem. 183 (2010) 1075–1082.
[28] S.K. Wilke, R.A. Lundberg, D.C. Dunand, Hierarchical structural changes during redox cycling of fe-based lamellar foams containing YSZ, CeO2, or ZrO2, ACS Appl. Mater. Interfaces 12 (2020) 27190–27201.
[29] S.K. Wilke, D.C. Dunand, Fe-Ni foams self-heal during redox cycling: via reversible formation/homogenization of a ductile Ni scaffold, J. Mater. Chem. A Mater. 8 (2020) 19375–19386.
[30] S.M. Pennell, J.B. Mack, D.C Dunand, Evolution of lamellar architecture and microstructure during redox cycling of Fe-Co and Fe-Cu foams, J. Alloy. Compd. 918 (2022), 165606.
[31] J.B. Mack, S.M. Pennell, D.C. Dunand, Microstructural evolution of lamellar Fe-25Ni foams during steam-hydrogen redox cycling, Acta Mater. 237 (2022), 118148.
[32] C. Stolze, T. Janoschka, U.S. Schubert, F.A. Müller, S. Flauder, Directional solidification with constant ice front velocity in the ice-templating process, Adv. Eng. Mater. 18 (2016) 111–120, https://doi.org/10.1002/adem.201500235. Preprint at.
[33] R. Dougherty, K.-H. Kunzelmann, Computing local thickness of 3D structures with image, J. Microsc. Microanal. 13 (2007) 1678–1679.
[34] Erb, D. pybaselines: A Python library of algorithms for the baseline correction of experimental data (2022).
[35] K.M. Thyng, C.A. Greene, R.D. Hetland, H.M. Zimmerle, S.F DiMarco, True colors of oceanography, Oceanography 29 (2016) 9–13.
[36] Newville, Matthew et al. (2014). LMFIT: non-linear least-square minimization and curve-fitting for python.
[37] B.H. Toby, R.B. Von Dreele, GSAS-II: the genesis of a modern open-source all purpose crystallography software package, J. Appl. Cryst. 46 (2013) 544–549.
[38] S.K. Wilke, J.B. Mack, C. Kenel, D.C. Dunand, Evolution of directionally freeze-cast Fe2O3 and Fe2O3+NiO green bodies during reduction and sintering to create lamellar Fe and Fe-20Ni foams, J. Alloy. Compd. 889 (2022), 161707.
[39] C. Kenel, N.P.M. Casati, D.C. Dunand, 3D ink-extrusion additive manufacturing of CoCrFeNi high-entropy alloy micro-lattices, Nat. Commun. 10 (2019) 1–8. *2019 10:1*.
[40] O. Kubaschewski, Iron - Binary Phase Diagrams. Materials Engineering, 2, Springer-Verlag Heidelberg GmbH, 1982.
[41] A. Ferndndez Guillermet, The Fe-Mo (iron-molybdenum) system, Bull. Alloy Ph. Digrams 3 (1982).
[42] K. Koyama, M. Morishita, T. Harada, et al., Determination of standard gibbs energies of formation of $Fe_2Mo_3O_{12}$, $Fe_2Mo_3O_8$, Fe_2MoO_4, and $FeMoO_4$ of the Fe-Mo-O ternary system and μ phase of the Fe-Mo binary system by electromotive force measurement using a Y_2O_3-stabilized ZrO_2 solid electrolyte, Metall. Mater. Trans. B 34 (2003) 653–659.
[43] M. Hasegawa, Ellingham diagram, Treatise Process Metall. 1 (2014) 507–516.
[44] A.T. Nelson, E.S. Sooby, Y.J. Kim, B. Cheng, S.A Maloy, High temperature oxidation of molybdenum in water vapor environments, J. Nucl. Mater. 448 (2014) 441–447.
[45] K. Narwankar, F.E. Lange, C.G. Levi, Microstructure evolution of Zr0,-(Fe,O, A120,) materials synthesized with solution precursors, J. Am. Ceram. Soc. 80 (1997) 1684–1690.
[46] J.D. French, M.P. Harmer, H.M. Chan, G.A Miller, Coarsening-resistant dual-phase interprenetrating microstructures, J. Am. Ceram. Soc. 73 (1990) 2508–2510.
[47] R. Morales, D. Sichen, S. Seetharaman, et al., Reduction of Fe_2MoO_4 by hydrogen gas, Metall. Mater. Trans. B 33 (2002) 589–594.
[48] J. Eigen, B. Rutjens, M. Schroeder, Partial redox cycling of composite storage materials for rechargeable oxide batteries, J. Energy Storage 43 (2021), 103161.